Laminar fiber architecture and three-dimensional systolic mechanics in canine ventricular myocardium

KEVIN D. COSTA,[1] YASUO TAKAYAMA,[2] ANDREW D. McCULLOCH,[3] AND JAMES W. COVELL[4]

[1]*Department of Biomedical Engineering, Washington University, St. Louis, Missouri 63110;* [2]*Department of Internal Medicine, Kansai Medical University, Kyoto, Japan; and Departments of* [3]*Bioengineering and* [4]*Medicine, University of California, San Diego, La Jolla, California 92093*

Costa, Kevin D., Yasuo Takayama, Andrew D. McCulloch, and James W. Covell. Laminar fiber architecture and three-dimensional systolic mechanics in canine ventricular myocardium. *Am. J. Physiol.* 276 (*Heart Circ. Physiol.* 45): H595–H607, 1999.—Previous studies suggest that the laminar architecture of left ventricular myocardium may be critical for normal ventricular mechanics. However, systolic three-dimensional deformation of the laminae has never been measured. Therefore, end-systolic finite strains relative to end diastole, from biplane radiography of transmural markers near the apex and base of the anesthetized open-chest canine anterior left ventricular free wall ($n = 6$), were referred to three-dimensional laminar microstructural axes reconstructed from histology. Whereas fiber shortening was uniform [-0.07 ± 0.04 (SD)], radial wall thickening increased from base (0.10 ± 0.09) to apex (0.14 ± 0.13). Extension of the laminae transverse to the muscle fibers also increased from base (0.08 ± 0.07) to apex (0.11 ± 0.08), and interlaminar shear changed sign [0.05 ± 0.07 (base) and -0.07 ± 0.09 (apex)], reflecting variations in laminar architecture. Nevertheless, the apex and base were similar in that at each site laminar extension and shear contributed ~60 and 40%, respectively, of mean transmural thickening. Kinematic considerations suggest that these dual wall-thickening mechanisms may have distinct ultrastructural origins.

cleavage planes; cardiac mechanics; finite strain; wall thickening; regional

MORPHOLOGICAL STUDIES of ventricular myocardium reveal a syncytium of myocytes organized into branching laminar "sheets," which are approximately four cells thick and roughly stacked from apex to base (19, 34). A network of extracellular collagen fibers appears to provide tight coupling of myocytes within the sheet and looser coupling between adjacent sheets (5, 19). Potential spaces between the laminae give rise to "cleavage planes" in long- and short-axis sections of the mammalian heart (11, 16, 18, 35), and these exhibit substantial transmural and regional variations in orientation (19, 20).

The functional significance of this laminar architecture is not well understood. However, recent work from this laboratory by LeGrice and co-workers (20) indicates that a primary role may be to allow rearrangement of myofiber bundles by sliding along cleavage planes during the cardiac cycle. This may arise from reorientation of cleavage planes toward the radial direction with increased wall thickness, as observed in contracted (11, 18) and passively unloaded (35) ventricles. Such rearrangement is also consistent with an increased number of myocytes spanning the ventricular wall thickness (17, 35) and with transverse shear deformations measured in dogs (10, 29, 39, 40) and humans (4, 43) during systole. LeGrice and co-workers also showed that reorientation of longitudinal-radial (i.e., long-axis) cleavage planes due to transverse shear could account for the majority of end-systolic wall-thickening strain in the inner one-third of the canine midanterior left ventricular (LV) free wall and septum. However, the source of the remaining thickening in the subendocardium and outer two-thirds of the LV wall and the role of circumferential-radial (i.e., short-axis) cleavage planes and transverse shears were not explained.

Systolic radial thickening is of particular interest as a functional measure because of its significant contribution to stroke volume (8, 15) and its sensitivity to local changes in perfusion (13) and metabolism (31). Although myofiber contraction is the basis of ventricular function, several studies point out that the increase in myocyte diameter due to fiber shortening accounts for only a small fraction of systolic wall thickening (20, 32, 35). Furthermore, whereas fiber shortening is similar at the epicardium and endocardium (21, 32, 40) and also from apex to base (32), local wall thickening increases significantly from subepicardium to subendocardium (14, 32, 33, 40) and may also be greater at the apex and midventricle than at the base (3, 32, 38). In fact, Rademakers and co-workers (32), using magnetic resonance image (MRI) tagging in the closed-chest dog, showed no correlation between fiber strain and wall thickening. On the other hand, they found a significant correlation between regional thickening and endocardial cross-fiber shortening. Rearrangement of laminar myocardium has also been suggested to explain the paradoxically large cross-fiber shortening (21, 32, 40), but the specific mechanisms remain unclear.

To fully comprehend the functional role of laminar myocardium, an analysis of the three-dimensional (3-D) mechanics of the laminae is required. However, no studies have actually measured systolic deformations of myocardial laminae. We hypothesize that, in addition to sliding of adjacent sheets due to interlaminar shear, sheets of myocardium are dynamic structures that deform (i.e., extend and/or shorten) during systole and that both mechanisms are important for normal regional ventricular function. Measurements of trans-

The costs of publication of this article were defrayed in part by the payment of page charges. The article must therefore be hereby marked "*advertisement*" in accordance with 18 U.S.C. Section 1734 solely to indicate this fact.

mural end-systolic finite strains were referred to 3-D sheet microstructural axes reconstructed from histology near the apex and base of the canine anterior LV free wall. These two regions have distinct cleavage-plane anatomy (19) and differences in wall thickening (3, 32) but similar in-plane mechanics in terms of principal strain (2) and fiber shortening (32) and thus provide a unique opportunity to test our hypothesis. The findings revealed that the transverse shear associated with reorientation of sheets around the local fiber axis, as opposed to reorientation of long- or short-axis cleavage planes, contributes to LV wall thickening and cross-fiber shortening strains. In addition, we found substantial laminar extension transverse to the muscle fibers that varied transmurally and regionally and was the dominant source of radial thickening across the wall, which has not previously been shown. Kinematic considerations suggest that sheet extension and shear may have distinct ultrastructural origins critically dependent on the hierarchical organization of the collagen extracellular matrix.

METHODS

All animal studies were performed according to National Institutes of Health guidelines for the care and use of laboratory animals in research. All protocols were approved by the Animal Subjects Committee of the University of California, San Diego, which is accredited by the American Association for Accreditation of Laboratory Animal Care.

Surgical preparation. Six adult mongrel dogs (19–27 kg) were anesthetized to a surgical plane with pentobarbital sodium (25 mg/kg, with additional 50–100 mg/h), intubated, and ventilated with room air. The heart was exposed via median sternotomy and left fourth intercostal space thoracotomy and suspended in a pericardial cradle. A limb-lead electrocardiogram (ECG) was continuously recorded. Aortic pressure was monitored with a fluid-filled 120-cm 7-F pigtail catheter inserted into the right femoral artery and connected to a gauge (model P23XL, Spectramed-Statham). LV pressure was recorded with a micromanometer (model P6, Konigsberg) inserted through a stab wound in the apex, and the recorded pressure was matched with that from the pigtail catheter advanced into the LV.

To measure 3-D myocardial deformation in each heart, the LV long axis was defined using 1.6-mm-diameter lead beads sutured to the epicardium at the origin of the left main coronary artery and the apical dimple. Marker implantation sites were selected approximately one-fourth (basal site) and three-fourths (apical site) of the distance from base to apex measured along the LV long axis in a region midway between the left anterior papillary muscle and the anterior interventricular sulcus (Fig. 1*A*). Each marker array, or "bead set," consisted of three transmural columns of four to six 1-mm-diameter gold beads implanted using a stainless steel trocar, as described previously (39), with a 1.6-mm lead marker sewn to the epicardium above each column. For each of the two bead sets, the three epicardial surface markers and two long-axis markers were used to define a system of local "cardiac coordinates" $\{X_1, X_2, X_3\}$ aligned with the circumferential, longitudinal, and radial axes of the LV wall (25), respectively, as determined separately at the basal and apical measurement sites. Because these coordinate systems are defined by the local epicardial-tangent plane, curvature of the LV wall is accounted for.

Experimental protocol. The animal was positioned in a biplane X-ray system with image planes adjusted so all radiopaque markers were visible in both views. End-diastolic pressure was adjusted to 8–10 mmHg by inferior vena cava occlusion or infusion of warm saline via a catheter in the right femoral vein as needed. With the respirator turned off at end expiration, biplane images were recorded for several heartbeats using high-speed asynchronous cineradiography (16-mm film, 120 frames/s). During each run, ECG, aortic pressure, LV pressure, and camera shutter pulses were recorded on an eight-channel chart recorder (Brush-Clevelite, model 2000, Gould). At the end of the experiment, snares were placed around lung hila and inflow and outflow vessels from the heart. An overdose of pentobarbital sodium was administered, and the heart was brought to anoxic arrest by tightening the ligatures around the inflow vessels. Pressure in the LV was adjusted to 8–10 mmHg by injection of saline into the LV cavity, the right ventricle was vented, and the heart was fixed by retrograde aortic perfusion with buffered glutaraldehyde (2.5%) (41). The heart was excised and stored in 10% buffered Formalin for 24–48 h. Finally, with the positions of the X-ray tubes and image intensifiers unchanged, a geometric phantom was recorded and later used to compute perspective transformations so that 3-D coordinates of myocardial markers could be reconstructed from the biplane images (22).

Histology. To avoid the distortional effects of dehydration and shrinkage associated with embedding, histological measurements were obtained using freshly fixed heart tissue. The initial gross-sectioning procedure followed that of LeGrice et al. (20). A transmural rectangular block of tissue containing the implanted marker columns was carefully removed from the ventricular wall at the apical and basal measurement sites, with the edges of the block cut parallel to the local circumferential, longitudinal, and radial axes of the LV as determined from the same epicardial markers used for the strain analysis. The transmural thickness of the block was measured. With a Plexiglas template to guide the blade, two 1-mm-thick transmural slices were cut from the block: one parallel to the longitudinal-radial (2-3) surface and one parallel to the circumferential-radial (1-3) surface (Fig. 1*B*). These thick slices, which revealed laminar tissue structures separated by gaps, or cleavage planes, were further sectioned for quantitative histology, as described below.

To measure transmural variations in the orientation of laminar structures in the longitudinal-radial plane, the 1-mm thick transmural slice from the (2-3) surface was mounted on an anodized aluminum block with a cyanoacrylate-based specimen adhesive. The aluminum block was secured in the specimen vice of a vibrating microtome (Vibratome 1000, Technical Products International), and transmural sections 50–100 μm thick were obtained with high-amplitude, slow-advance settings with use of a single-edge Teflon-coated razor blade held at a presentation angle of 20°. The specimen was carefully transferred to a glass slide and allowed to dry partially at room temperature for ~20 min. With use of a video camera (model DXC-151, Sony) mounted on a light microscope (Optiphot-2, Nikon), video images of the tissue section at low-power (×30) magnification were acquired onto a microcomputer (Macintosh Quadra 900, Apple) with image-processing software (NIH Image 1.47), yielding an image resolution of 78 pixels/mm in the transmural direction. The dimensions of the wall thickness generally exceeded the field of view, so two separate images of each tissue section were acquired. The software allowed accurate registration and combination of the two images. Myocardial laminae and the cleavage planes separating them were visible with no further enhancement of the digital montage (Fig. 2). At each 1-mm

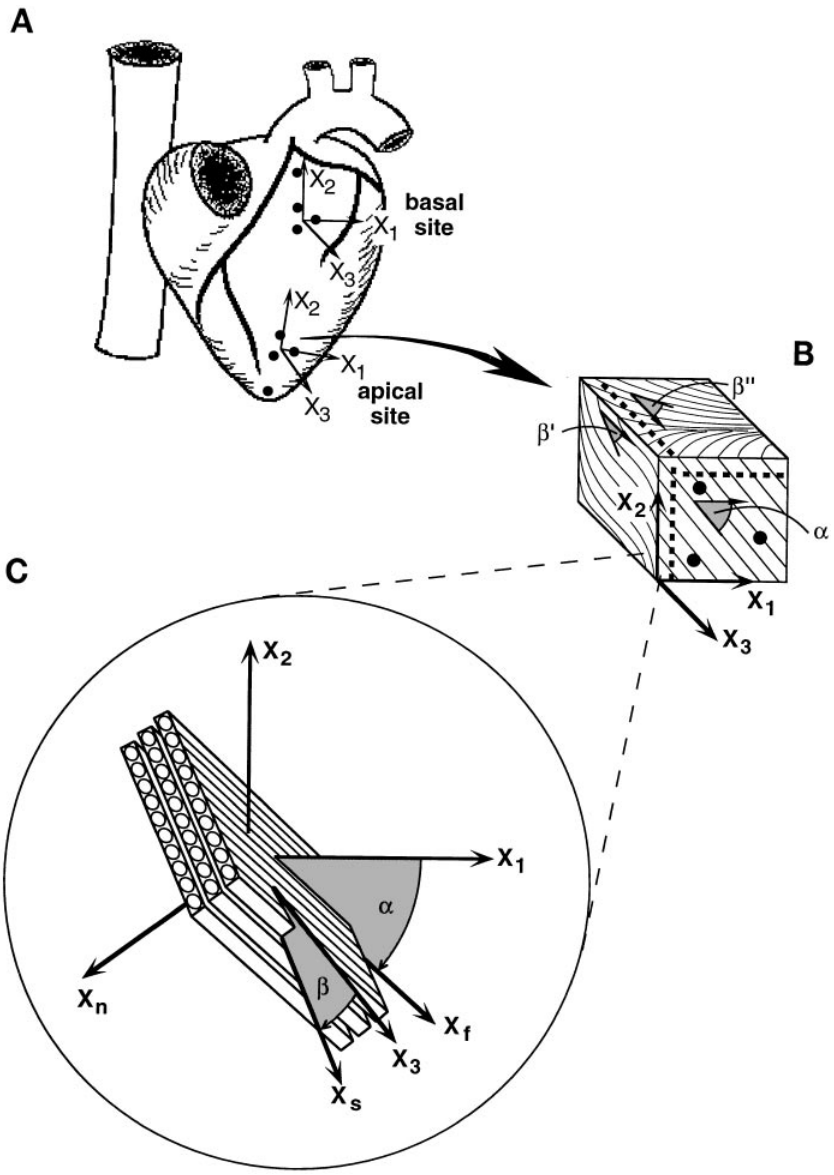

Fig. 1. Method for defining fiber-sheet coordinate system. *A*: epicardial markers used to define cardiac coordinates aligned with local circumferential (X_1), longitudinal (X_2), and radial (X_3) axes of left ventricle (LV) at apical and basal measurement sites. *B*: excised block of tissue containing bead set and used to measure transmural laminar morphology. Fiber angle (α) is measured from serial sections cut parallel to (1-2) plane. Cleavage-plane angles (β′ and β″) are measured from transverse sections (dashed lines) cut parallel to (2-3) and (1-3) planes, respectively. *C*: at a given transmural depth, measured angles are used to compute sheet angle (β), which together with α defines local "fiber-sheet coordinates" consisting of fiber axis (X_f), sheet axis perpendicular to X_f within sheet plane (X_s), and axis normal to sheet plane (X_n).

increment across the wall thickness from epicardium to endocardium (including the trabeculate layer), a mean cleavage-plane orientation (β′) was calculated from five angle measurements on the image within a 1.5-mm band along one edge of the tissue section; an angle of 0° was defined as parallel to the X_3 axis, and a counterclockwise rotation was represented by a positive angle. The process was repeated using the 1-mm-thick transmural tissue slice from the (1-3) plane to obtain the transmural distribution of the circumferential-radial cleavage-plane angle (β″) along the adjacent edge of the tissue section (Fig. 1*B*).

The remainder of the original transmural block of tissue was sliced into 1-mm-thick sections parallel to the circumferential-longitudinal (1-2) plane, forming a series from epicardium to endocardium used to measure the fiber-angle variation through the wall. Digitized video micrographs of each section were acquired as described above but under reflected light from an external source. The angle between the local muscle fiber axis and the circumferential edge of the tissue section was measured at nine sites on each image in the corner of the tissue section, and the mean fiber angle (α) was calculated at each transmural depth. The X_1 axis represented 0°, with a positive fiber angle representing a counterclockwise rotation. By making measurements along a single edge of the tissue block (Fig. 1*B*), corresponding fiber- and cleavage-plane angle data at a given depth represented the laminar architecture in ~5 mm^3 of myocardium, sampled from the same region where strains were measured.

Strain analysis. Data from a single heartbeat were selected for each animal so that end-diastolic pressure closely matched (within about ±1 mmHg) LV pressure during perfusion fixation of the heart. At each apical and basal measurement site, 3-D coordinates of the implanted markers in their end-diastolic and end-systolic configurations were computed from biplane X-ray images of the two-dimensional bead projections (22). End diastole and end systole were defined by the X-ray frames closest in time to the peak of the R wave of the ECG and the nadir of the dicrotic notch in the aortic pressure signal, respectively. With the 3-D marker coordinates at each site, a least-squares quadratic finite-element analysis was used to compute continuous transmural distributions of 3-D Lagrangian finite strains (7, 24), which describe the myocardial deformation at end systole with respect to an undeformed reference state defined to be end diastole. In

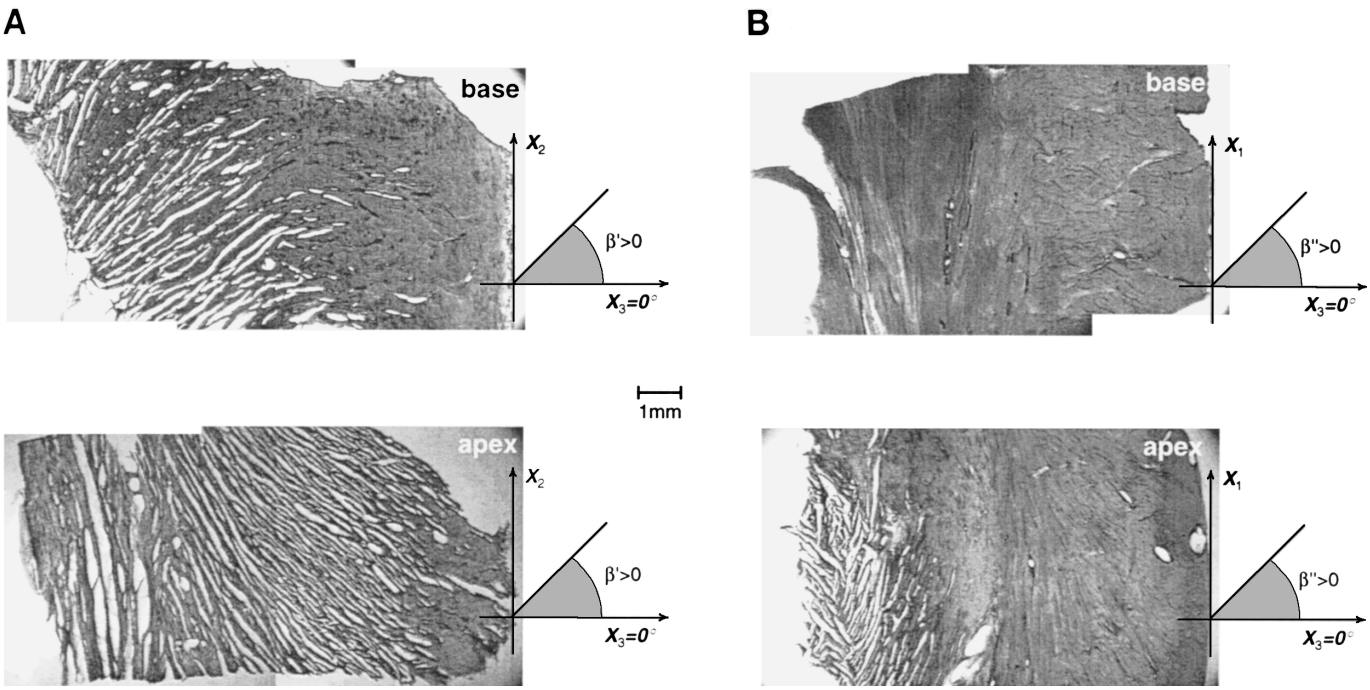

Fig. 2. Images of laminar cleavage planes in longitudinal-radial (*A*) and circumferential-radial (*B*) tissue sections from basal and apical measurement sites in anterior LV free wall. Each image is a montage of 2 video micrographs acquired under ×30 magnification. Orientation of specimen is indicated by cardiac coordinate axes X_1, X_2, and X_3, with endocardium to *left* and epicardium to *right*. *Study AF3*; LV pressure during fixation, 8 mmHg; section thickness, 50 μm; scale bar, 1 mm.

cardiac coordinates $[X_1, X_2, X_3]$, the three normal strain components measure myocardial stretch or shortening along the circumferential (E_{11}), longitudinal (E_{22}), and radial (E_{33}) cardiac axes. The three shear strains (E_{12}, E_{13}, and E_{23}) represent angle changes between pairs of the initially orthogonal coordinate axes. The strains were interpolated along the centroid of the deformed finite element at 10% increments of relative wall depth from the epicardium at each measurement site, and strains were not extrapolated beyond the depth of the most subendocardial beads.

The following model of the 3-D laminar architecture of ventricular myocardium has been described in detail elsewhere (7, 19, 20). To investigate the kinematic consequences of assuming this architecture, end-systolic strains at a given point in the LV wall were related to the local 3-D structural axes of the myocardial laminae. This was accomplished using a previously described method (7) to construct a system of local "fiber-sheet coordinates" $[X_f, X_s, X_n]$ defining the muscle fiber axis (X_f), the sheet axis (X_s), which lies within the sheet plane and is perpendicular to X_f, and the orthogonal X_n axis oriented normal to the sheet plane (Fig. 1*C*). Briefly, a continuous transmural fiber-angle distribution was obtained from a linear least-squares fit to the measured fiber angles (α). Then each cleavage-plane angle measurement (β′ and β″), together with α interpolated at a matching wall depth, was used compute a sheet angle (β) at that depth from one of the following equations

$$\beta = \arctan(\cos\alpha \tan\beta') \quad (1a)$$

$$\beta = \arctan(-\sin\alpha \tan\beta'') \quad (1b)$$

resulting in two separate distributions of β. The final transmural distribution of β was estimated from a weighted quadratic least-squares fit to the two sets of data obtained from *Eq. 1*, *a* and *b*, with residuals weighted by the sine or cosine of α to account for the effect of the fiber orientation on the theoretical accuracy of the cleavage-plane angle measurement (7).

With values of α and β at a given depth obtained from the fitted transmural distributions, 3-D end-systolic strains (**E**) were transformed from cardiac coordinates to fiber-sheet coordinates by using the following equation (12)

$$\mathbf{E}^{(\text{fiber sheet})} = \mathbf{M}\mathbf{E}^{(\text{cardiac})}\mathbf{M}^{\mathrm{T}} \quad (2)$$

where $\mathbf{M}^{\mathrm{T}}$ is the transpose of the 3 × 3 coordinate transformation matrix given by $\mathbf{M} = [\cos\alpha, \sin\alpha, 0; -\sin\alpha\sin\beta, \cos\alpha\sin\beta, \cos\beta; \sin\alpha\cos\beta, -\cos\alpha\cos\beta, \sin\beta]$. The resulting "fiber-sheet strains" include stretch or shortening along the fiber (E_{ff}), sheet (E_{ss}), and normal (E_{nn}) directions and the three shear strains (E_{fs}, E_{fn}, and E_{sn}, respectively). Whereas E_{fs} describes shearing within the sheet plane, the other two shear strains may arise from a relative sliding of adjacent myocardial laminae parallel to the fiber axis (E_{fn}) or transverse to the fiber axis (E_{sn}). It follows that $S_{sheet} = \sqrt{E_{fn}^2 + E_{sn}^2}$ represents shear in the direction of maximum interlaminar sliding. The overall maximum shear strain (S_{max}) at any point equals one-half of the difference between the maximum and minimum principal strains (12). Comparison of S_{sheet} and S_{max} allows assessment of the contribution of interlaminar sliding to overall systolic shear strain.

Contributions of fiber-sheet strain to wall thickening. To examine the contributions of laminar deformation to systolic cardiac strains, the components of $\mathbf{E}^{(\text{cardiac})}$ may be solved in terms of $\mathbf{E}^{(\text{fiber sheet})}$ by inverting *Eq. 2*. In general, all six sheet strain components and the fiber and sheet angle may be involved in these relations. However, as the following equation reveals

$$E_{33} = E_{ss}\cos^2\beta + E_{nn}\sin^2\beta + 2E_{sn}\sin\beta\cos\beta \quad (3)$$

the radial wall-thickening strain (E_{33}) depends only on β and the fiber-sheet components of strain in the (X_s, X_n) plane perpendicular to the local fiber axis, namely E_{ss}, E_{nn}, and E_{sn}. The contribution of each term on the right-hand side of *Eq. 3* is investigated to assess the fiber-sheet strain determinants of systolic wall thickening.

Statistical analysis. Values are means ± SD unless otherwise specified. The effects of region (apex vs. base) and wall depth on each strain component were determined by two-factor ANOVA. The two-tailed *t*-test was used to compare each strain component at each region with a hypothesized mean value of zero. The effects of region and depth on the correlation between S_{max} and S_{sheet} were tested by two-way analysis of covariance. Statistics were performed using SuperANOVA version 1.11 and StatView version 4.01 software (both by Abacus Concepts, Berkeley, CA). Statistical significance was accepted at $P < 0.05$.

RESULTS

Mean hemodynamic parameters were as follows: heart rate 100 ± 11 beats/min, LV end-diastolic pressure 9 ± 2 mmHg, and LV end-systolic pressure 117 ± 34 mmHg. Mean LV pressure during glutaraldehyde fixation (9 ± 1 mmHg) was not significantly different from end-diastolic pressure. Therefore, the fiber- and cleavage-plane orientations measured in the fixed hearts were assumed to represent accurately the laminar tissue structure in the end-diastolic reference configuration. The basal and apical measurement sites were located 23 ± 6 and 80 ± 11%, respectively, of the distance from base to apex along the LV long axis, in a region of the anterior LV free wall ~2–4 cm septal of the anterior papillary muscle. Mean wall thickness was 12 ± 3 mm at the base and 10 ± 2 mm at the apex.

Fiber and sheet orientation. Figure 3 illustrates the transmural variations of the measured α, β′, and β″, which were very consistent from heart to heart at a given site but showed considerable regional variation from apex to base. At both sites, α spanned an ~120° range from epicardium to endocardium (Fig. 3, *A* and *B*, *top*), but the distribution was more symmetrical at the base, where circumferential fibers (α = 0°) were located near midwall compared with ~20% depth at the apex. The orientation of (2-3) cleavage planes (β′) at the apex

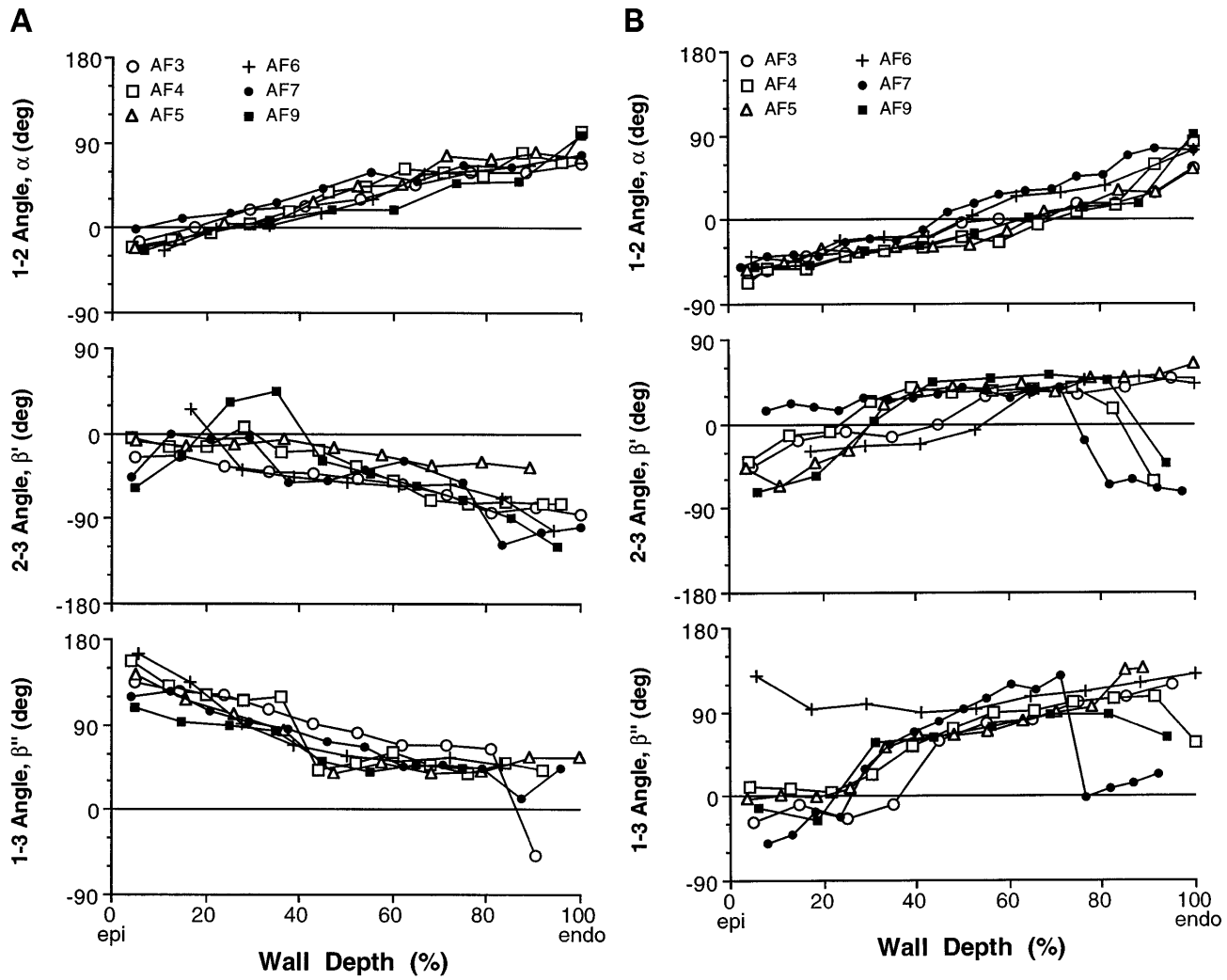

Fig. 3. Measured distributions of α, β′, and β″ vs. relative wall depth from all hearts at apical (*A*) and basal (*B*) sites. Each point represents average of several measurements at a given depth (α, $n = 9$; β′ and β″, $n = 5$). *AF3–7* and *AF9*, study designations; epi, epicardium; endo, endocardium.

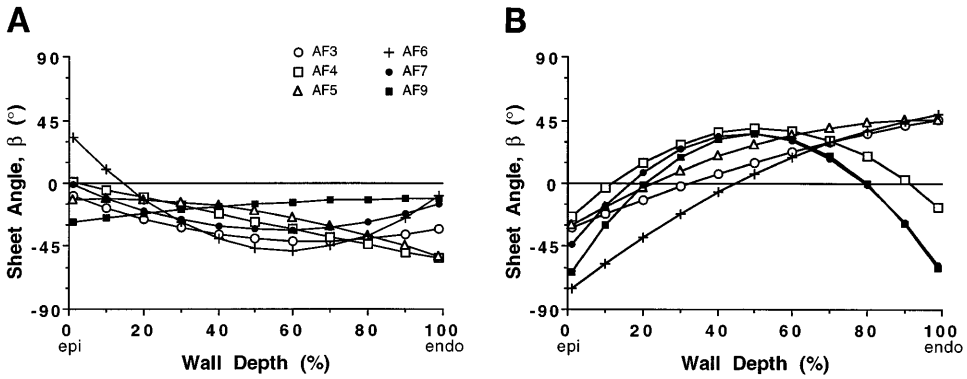

Fig. 4. Fitted transmural distributions of β from all hearts at apical (*A*) and basal (*B*) sites.

decreased from nearly radial (β′ = 0°) at the epicardium to nearly longitudinal (β′ = −90°) at the endocardium, whereas β′ at the base increased from about −45° at the epicardium to 45° in the midwall and endocardium (Fig. 3, *A* and *B*, *middle*). The opposite orientation of (2-3) cleavage planes between apex and base is clearly illustrated in Fig. 2*A*. The (1-3) angle (β″) crossed 90° near midwall at the two sites but again had opposite transmural gradients (Fig. 3, *A* and *B*, *bottom*) corresponding to a chevron pattern of the cleavage planes that fanned out from a circumferential orientation and was oppositely oriented at the apex compared with the base (Fig. 2*B*). In three hearts at the base and one at the apex, an abrupt change in sheet orientation at the compacta-trabeculata interface was indicated by a rapid change in β′ or β″ near the inner one-fourth of the wall. Such a transition is observed in Fig. 2*B*, *bottom*.

Fitted sheet-angle distributions at the apex and base of each heart are shown in Fig. 4. The average root-mean-squared error in the fit to β was 18.4 ± 8.2°, which was comparable to the variability of cleavage-plane angle measurements (~20°) and was not significantly improved by increasing the order of the fitted polynomial from quadratic to cubic. The sheet angle changed sign from negative at the apex to mainly positive at the base, but the magnitude of β′ did not usually exceed 45° in either region, indicating that the 3-D orientation of the myocardial sheet axis was predominantly radial.

Systolic strains in cardiac coordinates. Mean end-systolic strains referred to cardiac coordinates are shown in Fig. 5. Because not all bead sets spanned the entire wall thickness, mean values at the subendocardial depths were obtained from a reduced sample size. At the apex, mean circumferential shortening strain (E_{11}) exceeded longitudinal shortening (E_{22}), whereas E_{11} and E_{22} were comparable at the base. At both regions, radial thickening (E_{33}) was consistently the largest strain component in magnitude and gradient. The torsional shear strain (E_{12}) was uniform and positive. The circumferential-radial transverse shear strain (E_{13}) changed sign from apex to base. The mean longitudinal-radial transverse shear strain (E_{23}) was negative at the epicardium and positive in the subendocardium at both regions. All three cardiac shear strains were small (less than ±0.04) compared with the normal strain components, but only the mean value of E_{23} at the base was not significantly different from zero (P = 0.09).

All six cardiac strain components exhibited a significant effect of region (base vs. apex), and all except E_{12} and E_{13} had a significant wall depth effect. The only significant interaction between region and depth was

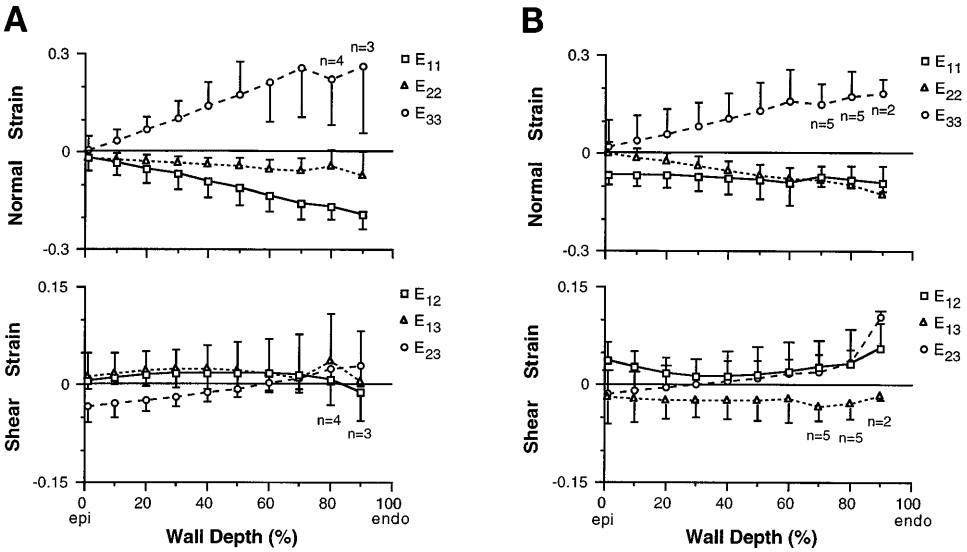

Fig. 5. Cardiac strain transmural distributions of mean end-systolic finite strains referred to local circumferential, longitudinal, and radial coordinates (X_1, X_2, and X_3), respectively, at apical (*A*) and basal (*B*) sites. Error bars, SD (n = 6, except as noted). Note different scales for shear and normal strains.

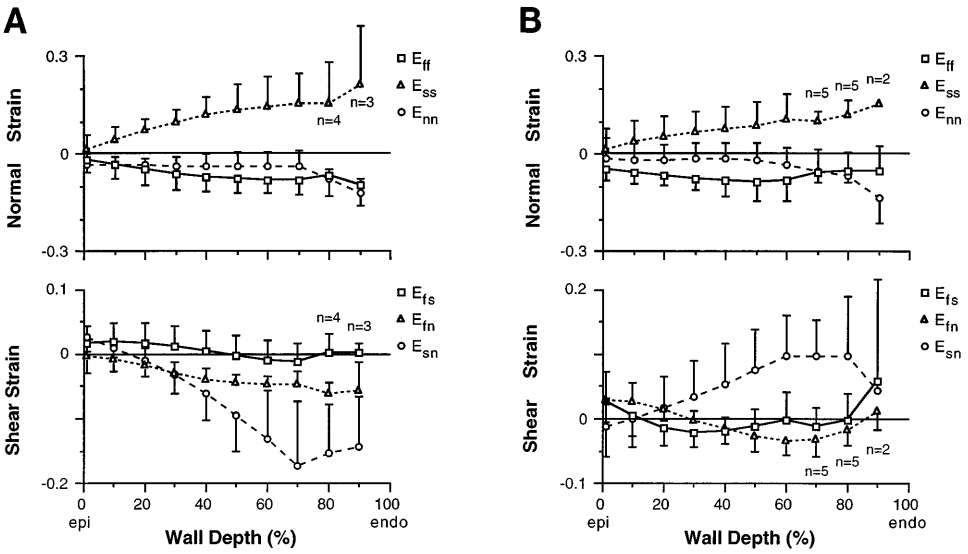

Fig. 6. Fiber-sheet strain transmural distributions of mean end-systolic finite strains referred to local fiber, sheet, and normal coordinates (X_f, X_s, and X_n), respectively, at apical (A) and basal (B) sites. Note large sheet extension (E_{ss}) and sheet-normal shear (E_{sn}), which changes sign from apex to base. Same format as Fig. 5.

for E_{11}, which was more uniform at the base than at the apex. There were no significant effects of region or depth ($P > 0.3$) on the determinant of the deformation gradient tensor (det**F**), which averaged 0.95 ± 0.06 (data not shown), indicating a 5% overall mean loss in tissue volume from end diastole to end systole.

Systolic strains in fiber-sheet coordinates. Mean end-systolic strains referred to fiber-sheet coordinates are shown in Fig. 6. Fiber strain (E_{ff}) was significant ($P < 0.0001$) and indicated a transmurally and regionally homogeneous 5–8% fiber shortening during systole. Similarly, negative E_{nn} indicated small but significant ($P < 0.0005$) shortening normal to the fiber-sheet plane, possibly reflecting thinning of the laminae. In contrast, the sheet strain (E_{ss}) was positive and increased transmurally from zero at the epicardium, indicating substantial (10–20%) extension of the sheet plane transverse to the muscle fiber axis. Shear strain within the sheet plane (E_{fs}) was not significantly different from zero at the apex or base ($P > 0.25$). A small negative E_{fn} at the apex suggested some relative sliding of adjacent myocardial laminae parallel to the fiber axis, but mean E_{fn} was not significant at the base ($P = 0.31$). Far greater sliding transverse to the fiber axis was indicated by the dominant E_{sn} component, particularly in the inner one-half of the wall where the magnitude of E_{sn} was ~0.10 at the base and 0.15 at the apex, similar to E_{ss}. Also, the sign of E_{sn} changed from positive at the base to negative at the apex, similar to β. Statistically, only E_{ss}, E_{sn}, and E_{fn} differed in magnitude from apex to base (all were greater at the apex), there were no significant interactions between the effects of region and depth, and the depth effect was not significant for E_{ff} ($P = 0.13$) or E_{fs} ($P = 0.058$).

Maximum end-systolic shear strain. S_{sheet} and S_{max} exhibited a significant effect of depth ($P = 0.0001$), increasing from epicardium to endocardium (data not shown). However, the regional variation was not significant. Two-way analysis of covariance revealed a strong dependence of S_{max} on S_{sheet} ($P < 0.0001$), with no significant interaction of region ($P = 0.077$) or depth ($P = 0.9$). Post hoc regression by using data from both regions and all depths (Fig. 7) had a slope of 1.00 ± 0.05 (SE), a small but significant intercept of 0.05 ± 0.005 (SE; $P < 0.0001$), and a correlation coefficient (r^2) of 0.81. The overall mean value of S_{sheet} was 0.08 ± 0.06 ($n = 109$), or ~60% of the overall mean value of S_{max} (0.13 ± 0.07).

Contributions of fiber-sheet strain to wall thickening. Considering the shear term in *Eq. 3*, positive values of $E_{sn}\sin\beta\cos\beta$ act to increase E_{33} and negative values decrease E_{33}. Therefore, because the sheet angle was in the range $-90° < \beta < 90°$, E_{sn} must have the same sign as β for $E_{sn}\sin\beta\cos\beta$ to augment wall thickening. Figure 8 indicates that this was a consistent trend at the apex and base [data labeled "midanterior" and "septum" were derived from a previous study (20); see DISCUSSION]. Data from the apical region were concen-

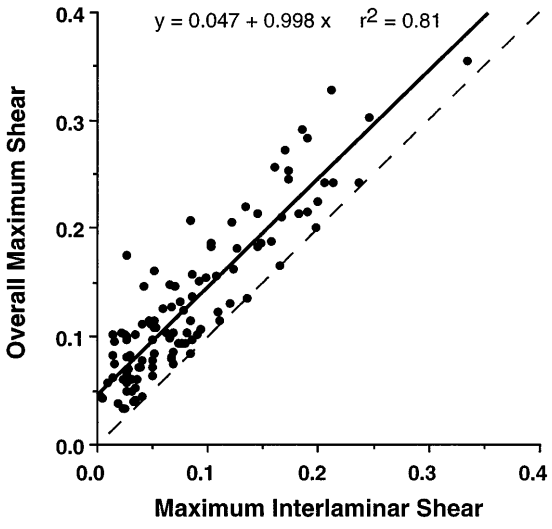

Fig. 7. Linear regression (solid line, with equation and correlation coefficient) indicates strong dependence of overall maximum shear strain (S_{max}) on maximum shear between adjacent myocardial sheets (S_{sheet}). Dashed line, unity slope with zero intercept. Data from all depths at apical and basal regions are represented ($n = 109$).

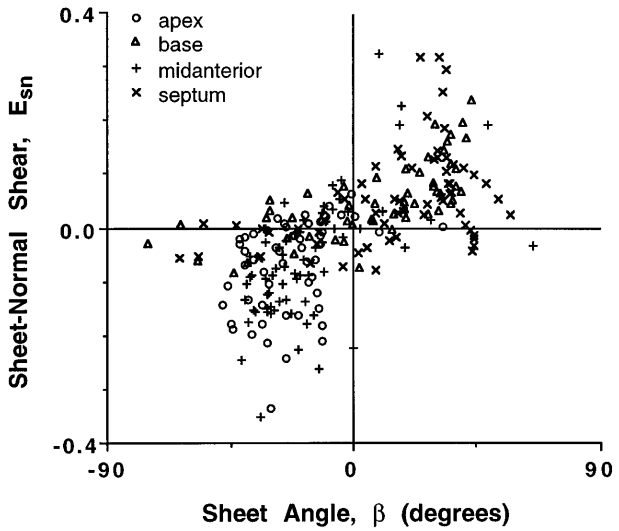

Fig. 8. Scatterplot of E_{sn} vs. reconstructed β from all depths at 4 regions of canine LV. Apex and base data from present study; midanterior and septum data from LeGrice et al. (20). Note globally consistent trend for E_{sn} and β to have same sign, and $|\beta| < 45°$.

trated in the quadrant where E_{sn} and β are negative; basal data fell primarily in the quadrant where E_{sn} and β are positive. Linear regression indicated a significant correlation between shear strain and β ($P < 0.0001$, $r^2 = 0.47$).

To assess the contributions of fiber-sheet strains to systolic wall thickening, the mean transmural distribution of each of the three terms on the right-hand side of *Eq. 3* was plotted along with mean E_{33} from the apex and base (Fig. 9). At both sites the "$E_{nn}\sin^2\beta$" term was nearly zero across the wall, whereas the "$E_{ss}\cos^2\beta$" and "$2E_{sn}\sin\beta\cos\beta$" terms increased strongly with depth and were nearly equivalent in the inner one-half of the LV wall. Table 1 indicates the average transmural fractional contribution of the three terms to E_{33}. The shear term accounted for almost one-half of the radial strain at the apex and base. The remainder of E_{33} was due primarily to the sheet extension (E_{ss}) term, indicating that stretching of myocardial laminae transverse to the fiber axis is also an important mechanism for systolic wall thickening. These results were consistent between the apex and base despite regional differences in mean E_{33} ($P = 0.04$).

DISCUSSION

The objective of this study was to test the hypothesis that relative sliding of adjacent sheets of myocardium and deformations along sheet structural axes are each important mechanisms for normal regional ventricular function. Measurements indicated laminar deformations that have not previously been documented; these include sheet thinning and substantial laminar extension transverse to the muscle fibers, which varied transmurally and regionally. Also, there were large interlaminar transverse shear strains that changed sign from base to apex. Sheet extension and shear were the primary determinants of wall thickening strain, and their relative contributions were regionally consistent despite significant variations in radial thickening and laminar architecture. The ultrastructural basis of these findings and their functional implications are discussed below.

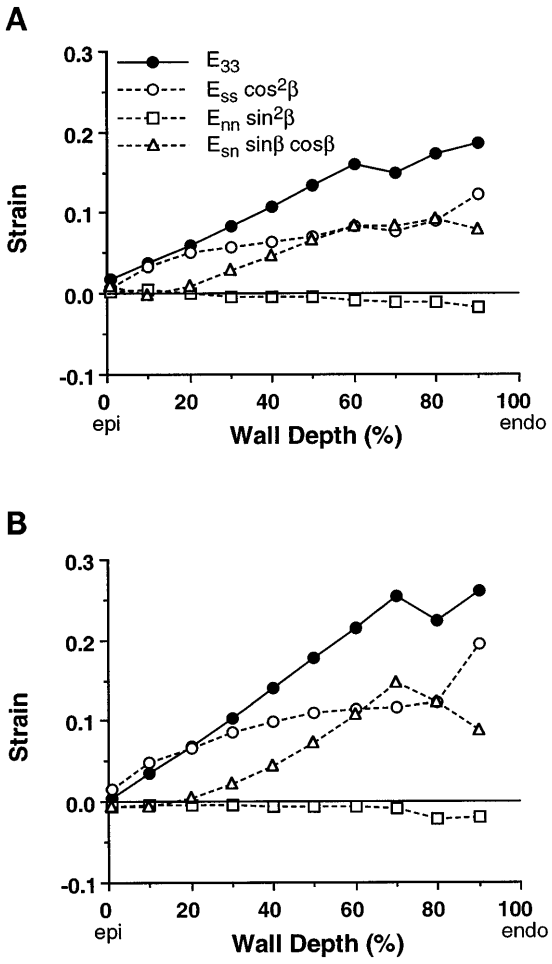

Fig. 9. Average transmural distributions, at basal (*A*) and apical (*B*) sites, of 3 fiber-sheet terms that contribute to radial thickening strain according to $E_{33} = E_{ss}\cos^2\beta + E_{nn}\sin^2\beta + 2E_{sn}\sin\beta\cos\beta$. E_{ss}, E_{nn}, and E_{sn}, systolic strains in sheet-normal transverse plane.

Fiber and sheet orientation. Our fiber-angle measurements indicated circumferential fibers located near midwall at the base but substantially closer to the

Table 1. *Transmural end-systolic radial strain and fractional fiber-sheet strain contributions to radial strain*

Region	E_{33}	Fractional Contributions to E_{33}*		
		$\frac{E_{ss}\cos^2\beta}{E_{33}}$	$\frac{E_{nn}\sin^2\beta}{E_{33}}$	$\frac{2E_{sn}\sin\beta\cos\beta}{E_{33}}$
Base	0.104 ± 0.090	0.59	−0.04	0.45
Apex	0.140 ± 0.126	0.66	−0.05	0.41
Midanterior‡	0.209 ± 0.188	0.64	0.01	0.31
Septum‡	0.112 ± 0.112	0.39	0.13	0.45

Values are means ± SD. *Fractional contributions to radial strain (E_{33}) were computed from ratios of corresponding overall mean transmural values from each region on the basis of *Eq. (3)*. ‡Data for midanterior and septum were derived from LeGrice et al. (20). E_{ss}, E_{nn}, and E_{sn}, systolic strains in sheet-normal transverse plane.

epicardium (~20% wall depth) at the apex. Although such a nonsymmetrical transmural distribution of apical fiber orientation is not well recognized, it is not entirely new. For example, although Streeter and colleagues (36, 37) emphasized that circumferential fibers occur midway between epicardium and endocardium throughout the entire LV wall, some of their classic work shows circumferential fibers at ~35% depth from the epicardium near the apex compared with 55% depth near the base (see Fig. 7*C* in Ref. 37). The comprehensive 3-D ventricular model of Nielsen et al. (27) also indicates considerable regional variability in fiber-angle orientation, although a trend toward apical asymmetry is not clear. On the other hand, LeGrice and co-workers from the same laboratory presented full longitudinal sections of LV myocardium showing subepicardial fiber angles that were much smaller in magnitude at the apex than at the midventricle and base (see Fig. 2*B* in Ref. 19), indicative of increasing transmural asymmetry toward the apex. Several previous studies from our laboratory (7, 23, 28, 40), in canine LV free wall locations between midventricle and apex, reported negative epicardial fiber angles of approximately one-half the magnitude of the positive endocardial angles, yielding circumferential fibers at ~30–40% wall depth. Therefore, there are substantial data consistent with an increasingly nonsymmetrical transmural distribution of fiber orientation from base to apex in the dog heart.

Published data on cleavage-plane orientations are far more limited. However, our transmural distributions of cleavage-plane angles (β′ and β″) at the apex were very consistent with corresponding data in the midanterior LV free wall of a dog heart fixed at similar inflation pressure (see Fig. 6*A* in Ref. 20) and with our previous data in stress-free myocardium (7). Regional apex-base variations in β′ were also similar to data reported by LeGrice and co-workers from the posterior LV free wall of two dog hearts fixed at zero transmural pressure (see Fig. 4*A* in Ref. 19). The roughly 30° offset in angle values between that study and ours may be an effect of inflation pressure or circumferential location. The chevron patterns observed in the circumferential-radial plane have also been previously described (16, 18, 20), and our data indicate a reversal of the chevron orientation from apex to base.

These histological measurements were used to reconstruct the 3-D orientation of myocardial laminae across the LV wall. Our approach differs from that of LeGrice et al. (20) in that the reliability of the computed sheet angle was incorporated into the reconstruction algorithm to account for expected discrepancies between β′ and β″. The theoretical basis for this analysis and examples of the resulting model fits have been given previously (7).

Regional heterogeneity in fiber and cleavage-plane orientations resulted in β that tended to be negative in the apical region and positive in the basal region. Nevertheless, β typically did not exceed ±45°, similar to our previous data in stress-free midanterior LV myocardium (7). Therefore, although the fiber and cleavage-plane angles may vary by 90–120° through the wall, the sheet angle is more consistent such that myocardial laminae are predominantly radial in orientation at end diastole. Differences between the actual 3-D sheet orientation and the "projected" two-dimensional cleavage-plane orientations have important implications for some proposed mechanisms of ventricular wall thickening (20, 35; see below).

Although cleavage-plane orientations generally varied smoothly from epicardium to endocardium, in several instances there was an abrupt change associated with the trabeculata-compacta interface (Fig. 3). Unfortunately, possible differences in mechanics between the compacta and trabeculata could not be specifically studied because of an insufficient number of markers for strain analysis within the trabeculate layer.

End-systolic strains. End-systolic finite strains in cardiac coordinates agreed with previous data from our laboratory (20, 39, 40) and others (4, 9, 26, 43). Nevertheless, all six cardiac strain components exhibited significant regional differences between apical and basal measurement sites. The decreased magnitude and gradient of circumferential shortening from apex to base has previously been shown using MRI tissue tagging in humans (6, 30). Waldman et al. (39) reported instances where longitudinal and circumferential shortening were comparable in magnitude, which we found to be a consistent trend at the base but not at the apex. Radial strain indicated greater wall thickening at the apex than at the base, consistent with recent 3-D MRI tagging studies in the closed-chest dog heart (3, 32). The circumferential-radial shear strain changed sign (but not magnitude) from apex to base, as predicted by Young et al. (42) on the basis of measurements of short-axis rotational displacements with use of MRI tagging in humans, possibly reflecting the opposite orientation of short-axis cleavage planes between the two sites. However, this contrasts with behavior in the long-axis plane where subendocardial β′ changed sign from apex to base, but the longitudinal-radial shear strain remained positive. Consequently, models of ventricular wall thickening based on reorientation of long-axis cleavage planes (20, 35) would predict subendocardial systolic wall thinning at the base, which is inconsistent with our data.

When strain components were referred to local fiber-sheet coordinates aligned with 3-D microstructural axes of myocardial laminae, much of the regional apex-base variation disappeared. In particular, fiber shortening (E_{ff}) was homogeneous transmurally and regionally, supporting some theoretical models of LV mechanics (1). Consequently, E_{33} was poorly correlated with E_{ff} across the wall ($r^2 = 0.20$), which has previously been shown at the endocardium and epicardium only (32). Other studies have shown similarity between inner- and outer-wall fiber shortening in dogs (32, 40) and humans (21), and Rademakers et al. (32) also found homogeneity of E_{ff} from apex to base, although there was significant variability around the LV circumference.

The data indicate that myocardial laminae also undergo substantial systolic deformations transverse to the fiber axis. Somewhat unexpectedly, E_{nn} was small but consistently negative, indicating shortening normal to the sheet plane (i.e., sheet thinning). Moreover, strain along the sheet axis (E_{ss}) indicated large extension of the laminae transverse to the muscle fibers. Another striking feature was the large sheet-normal shear strain (E_{sn}), which changed sign from apex to base concomitant with β. Of the three fiber-sheet strain components that exhibited significant regional effects, only E_{ss} and E_{sn} were strongly correlated with E_{33} (r^2 = 0.80, 0.77, and 0.12 for E_{ss}, $|E_{sn}|$, and E_{fn}, respectively). These findings are not easily explained by a simple increase in the diameter of myocytes within the sheet due to systolic fiber shortening. Alternative mechanisms based on the hierarchical organization of the collagen extracellular matrix are considered at the end of the DISCUSSION.

End-systolic shear strains. A recent study from this laboratory (20) concluded that relative sliding of adjacent myocardial laminae occurs primarily in the subendocardium, where the direction of maximum systolic shear is closely aligned with the local 3-D sheet orientation. However, substantial "slippage" of sheets might also be expected in the midwall where the transmural interlaminar branching density reaches a minimum (19). In the present study, we computed interlaminar shear (S_{sheet}) directly from the fiber-sheet strain data (E_{fn} and E_{sn}) and found a strong and consistent correlation between S_{sheet} and S_{max} that was statistically independent of wall depth. Specifically, S_{sheet} and S_{max} decreased in magnitude from endocardium to epicardium, which may reflect an increased interlaminar coupling in the subepicardium (19). However, S_{max} was always slightly greater than S_{sheet}, which contributed to the nonzero intercept in our regression analysis. Therefore, the relative contribution of S_{sheet} to S_{max} decreased from endocardium to epicardium, consistent with the maximum shear vector diverging from the sheet-normal vector, as reported previously (20). Nevertheless, although interlaminar shear (like most other systolic strain components) was largest in the subendocardium, it was also present in the midwall and subepicardium, indicating systolic slippage of the sheets across the entire LV wall.

In our correlation analysis, the small intercept may partially represent other noninterlaminar shear contributions to S_{max}, such as in-plane torsional shearing. In addition, because no shear strain can exceed S_{max}, any errors in S_{sheet} (i.e., in E_{fn} and E_{sn}) will skew the intercept away from zero. Consequently, the unity slope of the correlation suggests that S_{sheet} may actually represent a substantially greater percentage of S_{max} than the 60% overall mean contribution.

Contributions of sheet strain to wall thickening. Transverse shear (i.e., relative sliding) of myocardial laminae has previously been proposed as a mechanism for generating large changes in wall thickness during the cardiac cycle (20, 35). Our analysis reveals that it is the transverse shear associated with sliding of sheets lateral to the local fiber axis (E_{sn}), as opposed to the reorientation of long- or short-axis cleavage planes (E_{23} or E_{13}, respectively), that contributes to radial wall thickening strain (E_{33}). In addition, E_{33} also depends on β, as well as changes in sheet length and thickness due to E_{ss} and E_{nn}, respectively. Figure 10, which represents a region of laminar myocardium viewed in the plane perpendicular to the local fiber axis, helps visualize how each of these factors can locally alter wall thickness. We found that the relationship between E_{sn} and β was consistent with reorientation of myocardial laminae toward the radial direction during systole. Sheet extension lateral to the myofiber axis (E_{ss}) was also important, which has not previously been shown. At the apex and base, sheet extension and shear each contributed ~50% of E_{33} in the inner one-half of the wall, whereas sheet extension was the dominant mechanism in the outer wall.

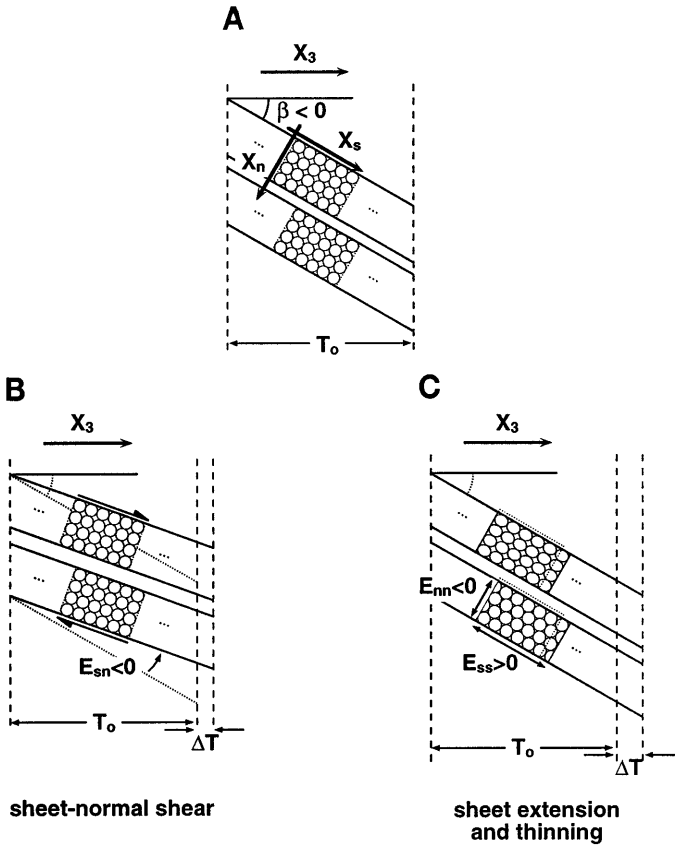

Fig. 10. Small region of myocardium viewed in sheet-normal (X_s, X_n) plane perpendicular to local fiber axis based on mean data from apical region at 60% wall depth. X_3 axis points from endocardium to epicardium. *A*: myocardial sheets at end diastole have negative sheet angle (β < 0) and are 4 cell diameters thick, and cells have circular cross section. *B*: at end systole, $E_{sn} < 0$ causes reorientation of sheets toward radial direction, one sheet slides relative to the other, and local wall thickness (T) increases by ΔT from initial value of T_0. *C*: wall thickness also increases, because end-systolic sheets are thinner ($E_{nn} < 0$) and longer ($E_{ss} > 0$) than at end diastole (dotted rectangle indicates end-diastolic dimensions). Myocytes have increased cross-sectional area because of fiber shortening. If myocytes do not rearrange, cell cross sections become elliptical (*top sheet*). If cells remain circular, average number of cells per sheet thickness decreases and cell count along sheet length increases reciprocally, indicating rearrangement of myocytes within sheet (*bottom sheet*).

To further test these mechanisms for wall thickening, the methods of the present investigation were used to reanalyze the tissue morphology and LV marker displacements measured by LeGrice et al. (20) from the canine midanterior LV free wall and septum. We have included these data in Fig. 8 and Table 1. The relationship between E_{sn} and β at these sites was consistent with our findings, with the midanterior wall being similar to the apex, whereas the septum was more like the base (Fig. 8). In terms of fractional contributions to E_{33} (Table 1), the midanterior results were similar to the apex and base: interlaminar shear was an important mechanism for wall thickening, but the contribution of sheet extension accounted for the majority of E_{33}. These findings indicate a highly consistent mechanism for systolic wall thickening in the LV free wall despite a twofold variation in mean E_{33}. Because of the more extensive surgical preparation in Ref. 20, the large midanterior thickening may not be simply a regional effect, particularly because greater wall thickening at the midventricle than at the apex is not consistent with recent MRI tagging studies (3, 32). In the septum, there was a reduced contribution from E_{ss}, compensated by a positive E_{nn} term, which accounted for 13% of E_{33} on average. This apparent regional difference in the wall-thickening mechanism may be a consequence of the unique functional role of the interventricular septum, where the "outer wall" is actually the pressure-loaded right ventricular subendocardium, or it may reflect the antisymmetrical mechanical behavior of the anterior-posterior and septal-lateral walls described by Azhari et al. (2).

A similar approach can be used to determine the fiber-sheet strain contributions to the paradoxically large systolic cross-fiber shortening strains, $E_{cc} < 0$, reported by several investigators (21, 32, 40). Similar to *Eq. 2*, the transformation equation relating fiber-sheet strains to fiber–cross-fiber strains yields the following relation

$$E_{cc} = E_{ss} \sin^2 \beta + E_{nn} \cos^2 \beta - 2E_{sn} \sin \beta \cos \beta \quad (4)$$

where the shear term is identical in magnitude to the shear term in *Eq. 3* and accounted for >75% of E_{cc} on average at the four measurement sites at which we have data. Therefore, the strong correlation between endocardial E_{cc} and E_{33} described by Rademakers and co-workers (32) probably arises from the fact that the same interlaminar shear mechanism contributes substantially to radial thickening and cross-fiber shortening.

Ultrastructural basis for the observed fiber-sheet strains. Our analysis averages the deformations determined from radiographic bead coordinate data and the corresponding histological measurements over several cubic millimeters. Unfortunately, it is not yet possible to directly measure the motion of myocardial laminae. However, because pathological processes may act to alter ventricular function by affecting laminar mechanics, it is interesting to speculate on the role of various laminar structures.

Shear within the sheet plane (E_{fs}) was not significant, suggesting that adjacent muscle fibers remain essentially parallel to one another during systole and do not slide along the fiber axis. This may reflect mechanical restriction by the extensive endomysial collagen network connecting myocytes within the laminar fiber bundles (5, 19, 34). In contrast, sheet-normal shear (E_{sn}) indicates a 10–20° change of myocardial sheet orientation in the subendocardium, which is within the range of longitudinal-radial cleavage-plane reorientation observed by Spotnitz et al. (35) during passive inflation of the rat LV. If a typical sheet is four myocytes thick at end diastole (19), this angle change is equivalent to a lateral displacement of 0.7–1.5 cell diameters per sheet thickness (Fig. 10*B*). Such motions would most likely be accommodated by the longer perimysial collagen strands connecting adjacent laminar cell bundles (5, 19). This assumes that E_{sn} is due to a gradient along the normal axis of deformation in the sheet direction (i.e., $\partial x_s/\partial X_n$). Alternatively, E_{sn} could arise from a gradient along the sheet axis of deformation in the normal direction (i.e., $\partial x_n/\partial X_s$). However, this would require parallel sheets of myocardium to become skewed. It is unlikely that this would occur, since the myocardial laminae in fresh tissue are tightly packed, and interlaminar gaps arise primarily from tissue shrinkage due to dehydration (19). Therefore, sliding of adjacent myocardial sheets along cleavage planes probably accounts for the consistently large sheet-normal shear strain and similarly for the smaller fiber-normal shear (E_{fn}).

We also measured significant shortening and extension of the myocardial laminae. If it is assumed that myocytes have a circular cross section (17, 18), the sheet is four cells thick at end diastole (19), individual cells are incompressible, and the number of cells within the sheet is constant, we calculated the change in cell cross-sectional shape or the cell rearrangement within the sheet that was consistent with the measured strains (Fig. 10*C*). If myocytes within the sheet do not rearrange during systole, then subepicardial cells could remain essentially circular, with a major-to-minor axis ratio (ellipticity) <1.1. However, in the subendocardium, sheet thinning ($E_{nn} < 0$) and lateral extension ($E_{ss} > 0$) would require myocyte cross sections to become distorted (ellipticity ~1.3). This is not consistent with measurements of cell cross-sectional shape in the canine LV midwall, which showed <5% change in myocyte ellipticity in contracted vs. dilated hearts (18).

Alternatively, if cell cross sections remain circular during systole, then sheet extension would require rearrangement of myocytes within the sheet, e.g., interdigitation. Specifically, an increase in cell diameter due to fiber shortening ($E_{ff} < 0$), combined with the observed sheet thinning ($E_{nn} < 0$), would lead to a decrease in the number of cells across the sheet thickness from 4 at end diastole to ~3.8 in the subepicardium and 3.5 in the subendocardium at end systole. There would also be a reciprocal increase in the number of cells along the sheet length of 5% in the subepicardium and 14% in the subendocardium, which, combined with the increased end-systolic cell diameter (3–4%), closely matches the measured sheet extension

based on E_{ss}. It is unclear whether apparent slackening of intermyocyte struts during systole (5) would allow such cellular rearrangement within the sheet plane. However, together with the reorientation of sheets toward the radial direction due to E_{sn}, this method of sheet extension is qualitatively consistent with published increases in transmural cell number and center-to-center distance with increasing ventricular wall thickness (17, 35).

Thus the two mechanisms that contribute most to systolic wall thickening may depend on different components of the hierarchical collagen extracellular matrix, with sheet extension regulated by the endomysial intralaminar network and interlaminar shear associated with the perimysial connections between adjacent sheets of myocardium.

In conclusion, we have demonstrated that normal LV mechanics involve considerable deformation of laminar sheets of myocardium. In the anterior LV free wall, the sheets become thinner from end diastole to end systole, and there is substantial sheet extension transverse to the muscle fibers that varies transmurally and regionally. Also, the laminae become more radially oriented because of interlaminar transverse shear strains, which represent the majority of overall systolic shear, and change sign from base to apex, reflecting regional differences in the underlying 3-D laminar architecture. Sheet extension and shear accounted for 60 and 40% of radial wall thickening strain, respectively, and also explained the transmural and regional variations in radial strain, which was poorly correlated with uniform systolic fiber shortening. The specific mechanisms by which myocyte contraction is converted to sheet extension and interlaminar shear remain to be identified. However, kinematic considerations suggest that sliding of adjacent myocardial sheets and rearrangement of myocytes within the laminae may be two cellular mechanisms responsible for the sheet strains that contribute to large ventricular wall thickening at end systole. The apparently distinct ultrastructural origins of sheet extension and shear may provide redundant mechanisms for sustaining LV function during pathological alterations of the collagen extracellular matrix.

We thank Rish Pavelec and Dr. Jeff Holmes for assistance with the experiments and Dr. Lewis Waldman for many stimulating and fruitful discussions. We are indebted to Dr. Ian LeGrice for sharing expertise and insight about the laminar structure of the myocardium and for generously providing raw histology and bead coordinate data from the midanterior and septal regions of the LV.

This research was supported by National Heart, Lung, and Blood Institute Grants HL-32583 (J. W. Covell) and HL-41603 (A. D. McCulloch) and National Science Foundation Grant BES-9634974. K. D. Costa was supported by National Heart, Lung, and Blood Institute Predoctoral Training Grant HL-07089 (S. Chien).

Address for reprint requests: J. W. Covell, UCSD School of Medicine, Dept. of Cardiology, 9500 Gilman Dr., Mail Code 0613J, La Jolla, CA 92093.

Received 11 May 1998; accepted in final form 15 October 1998.

REFERENCES

1. **Arts, T., P. C. Veenstra, and R. S. Reneman.** Epicardial deformation and left ventricular wall mechanics during ejection in the dog. *Am. J. Physiol.* 243 (*Heart Circ. Physiol.* 12): H379–H390, 1982.
2. **Azhari, H., J. L. Weiss, W. J. Rogers, C. O. Siu, E. A. Zerhouni, and E. P. Shapiro.** Noninvasive quantification of principal strains in normal canine hearts using tagged MRI images in 3-D. *Am. J. Physiol.* 264 (*Heart Circ. Physiol.* 33): H205–H216, 1993.
3. **Azhari, H., J. L. Weiss, and E. P. Shapiro.** Distribution of myocardial strains: an MRI study. *Adv. Exp. Med. Biol.* 382: 319–328, 1995.
4. **Buchalter, M. B., J. L. Weiss, W. J. Rogers, E. A. Zerhouni, M. L. Weisfeldt, R. Beyar, and E. P. Shapiro.** Noninvasive quantification of left ventricular rotational deformation in normal humans using magnetic resonance imaging myocardial tagging. *Circulation* 81: 1236–1244, 1990.
5. **Caulfield, J. B., and T. K. Borg.** The collagen network of the heart. *Lab. Invest.* 40: 364–371, 1979.
6. **Clark, N. R., N. Reichek, P. Bergey, E. A. Hoffman, D. Brownson, L. Palmon, and L. Axel.** Circumferential myocardial shortening in the normal human left ventricle: assessment by magnetic resonance imaging using spatial modulation of magnetization. *Circulation* 84: 67–74, 1991.
7. **Costa, K. D., K. D. May-Newman, D. Farr, W. G. O'Dell, A. D. McCulloch, and J. H. Omens.** Three-dimensional residual strain in midanterior canine left ventricle. *Am. J. Physiol.* 273 (*Heart Circ. Physiol.* 42): H1968–H1976, 1997.
8. **Dumesnil, J. G., and R. M. Shoucri.** Quantitative relationships between left ventricular ejection and wall thickening and geometry. *J. Appl. Physiol.* 70: 48–54, 1991.
9. **Fann, J. I., G. E. Sarris, N. B. Ingels, Jr., M. A. Niczyporuk, K. L. Yun, G. T. Daughters II, G. C. Derby, and D. C. Miller.** Regional epicardial and endocardial two-dimensional finite deformations in canine left ventricle. *Am. J. Physiol.* 261 (*Heart Circ. Physiol.* 30): H1402–H1410, 1991.
10. **Feigl, E. O., and D. L. Fry.** Intramural myocardial shear during the cardiac cycle. *Circ. Res.* 14: 536–540, 1964.
11. **Feneis, H.** Das Gefuge des Herzmuskels bei Systole und Diastole. *Morphol. Jahrb.* 89: 371–406, 1943.
12. **Fung, Y. C.** *Foundations of Solid Mechanics.* Englewood Cliffs, NJ: Prentice-Hall, 1965.
13. **Gallagher, K. P., R. A. Gerren, M. C. Stirling, M. Choy, R. C. Dysko, S. P. McManimon, and W. R. Dunham.** The distribution of functional impairment across the lateral border of acutely ischemic myocardium. *Circ. Res.* 58: 570–583, 1986.
14. **Gallagher, K. P., G. Osakada, M. Matsuzaki, M. Miller, W. S. Kemper, and J. Ross, Jr.** Nonuniformity of inner and outer systolic wall thickening in conscious dogs. *Am. J. Physiol.* 249 (*Heart Circ. Physiol.* 18): H241–H248, 1985.
15. **Gould, K. L., J. W. Kennedy, M. Frimer, G. H. Pollack, and H. T. Dodge.** Analysis of wall dynamics and directional components of left ventricular contraction in man. *Am. J. Cardiol.* 38: 322–331, 1976.
16. **Grimm, A. F., K. V. Katele, and H.-L. Lin.** Fiber bundle direction in the mammalian heart: an extension of the "nested shells" model. *Basic Res. Cardiol.* 71: 381–388, 1976.
17. **Hort, W.** Untersuchunged uber die Muskelfaserdehnung und das Gefuge des Myokards in der rechten Herzkammerwand des Meerschweinchens. *Virchows Arch.* 329: 694–731, 1957.
18. **Hort, W.** Makroskopische und mikrometrische Untersuchungen am Myokard verschieden stark gefullter linker Kammern. *Virchows Arch.* 329: 523–564, 1960.
19. **LeGrice, I. J., B. H. Smaill, L. Z. Chai, S. G. Edgar, J. B. Gavin, and P. J. Hunter.** Laminar structure of the heart: ventricular myocyte arrangement and connective tissue architecture in the dog. *Am. J. Physiol.* 269 (*Heart Circ. Physiol.* 38): H571–H582, 1995.
20. **LeGrice, I. J., Y. Takayama, and J. W. Covell.** Transverse shear along myocardial cleavage planes provides a mechanism for normal systolic wall thickening. *Circ. Res.* 77: 182–193, 1995.
21. **MacGowan, G. A., E. P. Shapiro, H. Azhari, C. O. Siu, P. S. Hees, G. M. Hutchins, J. L. Weiss, and F. E. Rademakers.** Noninvasive measurement of shortening in the fiber and cross-fiber directions in the normal human left ventricle and in idiopathic dilated cardiomyopathy. *Circulation* 96: 535–541, 1997.

22. **MacKay, S. A., M. J. Potel, and J. M. Rubin.** Graphics methods for tracking three-dimensional heart wall motion. *Comput. Biomed. Res.* 15: 455–473, 1982.
23. **May-Newman, K. D., J. H. Omens, R. S. Pavelec, and A. D. McCulloch.** Three-dimensional transmural mechanical interaction between the coronary vasculature and passive myocardium in the dog. *Circ. Res.* 74: 1166–1178, 1994.
24. **McCulloch, A. D., and J. H. Omens.** Non-homogeneous analysis of three-dimensional transmural finite deformation in canine ventricular myocardium. *J. Biomech.* 24: 539–548, 1991.
25. **Meier, G. D., M. C. Ziskin, W. P. Santamore, and A. A. Bove.** Kinematics of the beating heart. *IEEE Trans. Biomed. Eng.* 27: 319–329, 1980.
26. **Moore, C. C., W. G. O'Dell, E. R. McVeigh, and E. A. Zerhouni.** Calculation of three-dimensional left ventricular strains from biplanar tagged MR images. *J. Magn. Reson. Imaging* 2: 165–175, 1992.
27. **Nielsen, P. M. F., I. J. LeGrice, B. H. Smaill, and P. J. Hunter.** Mathematical model of geometry and fibrous structure of the heart. *Am. J. Physiol.* 260 (*Heart Circ. Physiol.* 29): H1365–H1378, 1991.
28. **Omens, J. H., K. D. May, and A. D. McCulloch.** Transmural distribution of three-dimensional strain in the isolated arrested canine left ventricle. *Am. J. Physiol.* 261 (*Heart Circ. Physiol.* 30): H918–H928, 1991.
29. **Osakada, G., S. Sasayama, C. Kawai, A. Hirakawa, W. S. Kemper, D. Franklin, and J. Ross, Jr.** The analysis of left ventricular wall thickness and shear by an ultrasonic triangulation technique in the dog. *Circ. Res.* 47: 173–181, 1980.
30. **Palmon, L. C., N. Reichek, S. B. Yeon, N. R. Clark, D. Brownson, E. Hoffman, and L. Axel.** Intramural myocardial shortening in hypertensive left ventricular hypertrophy with normal pump function. *Circulation* 89: 122–131, 1994.
31. **Perrone-Filardi, P., S. L. Bacharach, V. Dilsizian, S. Maurea, J. A. Frank, and R. O. Bonow.** Regional left ventricular wall thickening: relation to regional uptake of ^{18}fluorodeoxyglucose and ^{201}TI in patients with chronic coronary artery disease and left ventricular dysfunction. *Circulation* 86: 1125–1137, 1982.
32. **Rademakers, F. E., W. J. Rogers, W. H. Guier, G. M. Hutchins, C. O. Siu, M. L. Weisfeldt, J. L. Weiss, and E. P. Shapiro.** Relation of regional cross-fiber shortening to wall thickening in the intact heart: three-dimensional strain analysis by NMR tagging. *Circulation* 89: 1174–1182, 1994.
33. **Sabbah, H. N., M. Marzilli, and P. D. Stein.** The relative role of subendocardium and subepicardium in left ventricular mechanics. *Am. J. Physiol.* 240 (*Heart Circ. Physiol.* 9): H920–H926, 1981.
34. **Smaill, B. H., and P. J. Hunter.** Structure and function of the diastolic heart: material properties of passive myocardium. In: *Theory of Heart: Biomechanics, Biophysics and Nonlinear Dynamics of Cardiac Function*, edited by L. Glass, P. J. Hunter, and A. D. McCulloch. New York: Springer-Verlag, 1991, p. 1–29.
35. **Spotnitz, H. M., W. D. Spotnitz, T. S. Cottrell, D. Spiro, and E. H. Sonnenblick.** Cellular basis for volume-related wall thickness changes in the rat left ventricle. *J. Mol. Cell. Cardiol.* 6: 317–331, 1974.
36. **Streeter, D. D., Jr., W. E. Powers, M. A. Ross, and F. Torrent-Guasp.** Three-dimensional fiber orientation in the mammalian left ventricular wall. In: *Cardiovascular System Dynamics*, edited by J. Baan, A. Noordergraaf, and J. Raines. Cambridge, MA: MIT Press, 1978, p. 73–84.
37. **Streeter, D. D., Jr., H. M. Spotnitz, D. P. Patel, J. Ross, Jr., and E. H. Sonnenblick.** Fiber orientation in the canine left ventricle during diastole and systole. *Circ. Res.* 24: 339–347, 1969.
38. **Takeda, T., H. Toyama, N. Ishikawa, M. Satoh, T. Masuoka, R. Ajisaka, K. Iida, W. Jin, Y. Sugishita, and Y. Itai.** Quantitative phase analysis of myocardial wall thickening by technetium-99M 2-methoxy-isobutyl-isonitrile SPECT. *Ann. Nucl. Med.* 6: 69–78, 1992.
39. **Waldman, L. K., Y. C. Fung, and J. W. Covell.** Transmural myocardial deformation in the canine left ventricle: normal in vivo three-dimensional finite strains. *Circ. Res.* 57: 152–163, 1985.
40. **Waldman, L. K., D. Nossan, F. Villarreal, and J. W. Covell.** Relation between transmural deformation and local myofiber direction in canine left ventricle. *Circ. Res.* 63: 550–562, 1988.
41. **Yoran, C., J. W. Covell, and J. J. Ross.** Rapid fixation of the left ventricle: continuous angiographic and dynamic recordings. *J. Appl. Physiol.* 35: 155–157, 1973.
42. **Young, A. A., H. Imai, C.-N. Chang, and L. Axel.** Two-dimensional left ventricular deformation during systole using magnetic resonance imaging with spatial modulation of magnetization. *Circulation* 89: 740–752, 1994.
43. **Young, A. A., C. M. Kramer, V. A. Ferrari, L. Axel, and R. Reichek.** Three-dimensional left ventricular deformation in hypertrophic cardiomyopathy. *Circulation* 90: 854–867, 1994.